Chinese Chemical Letters 35 (2024) 109164

Contents lists available at ScienceDirect

Chinese Chemical Letters

journal homepage: www.elsevier.com/locate/cclet

Near-infrared double-cable conjugated polymers based on alkyl linkers with tunable length for single-component organic solar cells

Yikun Wang[a], Qiaomei Chen[a,*], Shijie Liang[a], Dongdong Xia[b], Chaowei Zhao[b], Christopher R. McNeill[c], Weiwei Li[a,*]

[a] Beijing Advanced Innovation Center for Soft Matter Science and Engineering & State Key Laboratory of Organic-Inorganic Composites, Beijing University of Chemical Technology, Beijing 100029, China
[b] Institute of Applied Chemistry, Jiangxi Academy of Sciences, Nanchang 330096, China
[c] Department of Materials Science and Engineering, Monash University, Wellington Road, Clayton, Victoria 3800, Australia

ARTICLE INFO

Article history:
Received 24 July 2023
Revised 25 September 2023
Accepted 28 September 2023
Available online 10 October 2023

Keywords:
Single-component organic solar cells
Double-cable conjugated polymers
Photovoltaic properties
Alkyl linkers

ABSTRACT

The photovoltaic properties of double-cable conjugated polymers are significantly influenced by the length of the alkyl linkers that connect donor backbones and acceptor side units. In this study, a series of 2-(3-oxo-2,3-dihydroinden-1-ylidene)malononitrile (IC)-based double-cable polymers with alkyl linkers ranging from C_8H_{16} to $C_{16}H_{32}$ (**Px**, x = 8, 10, 12, 14, 16) were synthesized for single-component organic solar cells (SCOSCs). Among these, the linker length x = 12 (**P12**) is found to optimize the power conversion efficiencies (PCEs) in SCOSCs. Specifically, PCEs increase from **P8** to **P12** and then decline from **P12** to **P16**. Detailed investigations of optical absorption, charge transport, and morphology provide insights into the underlying factors contributing to these PCE variations. The findings indicate that the exceptional photovoltaic properties observed in **P12** can be attributed to three key factors: A delicate balance between enhanced charge separation facilitated by the increased spacer length and reduced crystallinity resulting from longer spacers, higher charge mobilities, and well-balanced hole/electron transport characteristics. This study highlights the critical role of linker length in determining the photovoltaic properties of double-cable conjugated polymer-based SCOSCs and offers valuable guidance for the design of novel double-cable conjugated polymers.

Single-component organic solar cells (SCOSCs) have attracted increasing attention over the past five years due to their advantages of high thermal stability, simple solution processing, and homogenous thin films toward large-area fabrication [1–5]. This is because SCOSCs use one conjugated material as the photoactive layer, distinct from physically mixed blends of electron donor and electron acceptor materials in bulk-heterojunction (BHJ) OSCs. Single-component materials in SCOSCs were called “homojunction” conjugated materials, but they have difficulty in separating excitons into free charges and do not have separate channels for electron and hole transport. Therefore, homojunction-conjugated materials exhibit power conversion efficiencies (PCEs) below 3% due to strong charge recombination in SCOSCs [6]. The efficient alternative is to combine electron donor and electron acceptor units in one conjugated material, so that the driving force for exciton separation and separate channels for charge transport can be obtained. These materials include molecular dyads, diblock conjugated polymers, and double-cable conjugated polymers [7,8]. With the development of new single-component conjugated materials and new methods to tune phase separation in thin films [9,10], the PCE of SCOSCs has dramatically increased to over 13%. However, such PCEs still lag behind BHJOSCs which have achieved PCEs of over 19%, suggesting that the PCE of SCOSCs can be improved further with increased effort devoted to materials innovation and morphology optimization [11–18].

Double-cable conjugated polymers with conjugated polymer backbones as electron donors and aromatic side units as electron acceptors can efficiently absorb light and convert photo-excitation into free charges. These polymers can be universally designed with the consideration of conjugated backbones, acceptor side units, and also the linkers that connect the backbones and side units. For example, conjugated polymers backbones with different structures, from polythiophene derivatives [19], benzo[1,2-*c*:4,5-*c*′]dithiophene-4,8-dione [20], isoindigo [21], and diketopyrrolopyrrole [22,23] based polymers, have been applied into double-

* Corresponding authors.
E-mail addresses: chenqm@mail.buct.edu.cn (Q. Chen), liweiwei@iccas.ac.cn (W. Li).

https://doi.org/10.1016/j.cclet.2023.109164
1001-8417/

cable polymers with tunable absorption spectra. Another efficient method is to introduce different electron acceptors into the side units, such as fullerene [24], rylene diimides [25–28], non-fused electron acceptors [29–36], and Y-series acceptors [37]. The distinct nature of these electron acceptors enables double-cable polymers to show absorption spectra from 300 nm to 900 nm, so that PCE could be significantly enhanced to 13% for based Y-series acceptors [38].

Besides conjugated backbones and acceptor side units, the linkers between them play an important role to tune their phase separation in thin films. The length of the linkers is directly related to the distance between the backbones and acceptor side units. For example, in perylene diimide (PBI)-based double-cable polymers, the short alkyl linker C_6H_{12} results in a small distance, and hence severe charge recombination resulting in low short-circuit current density (J_{sc}) and low fill factor (FF). When C_6H_{12} was replaced by $C_{12}H_{24}$, charge recombination was reduced and hence the PCE was enhanced due to the larger distance between the backbone (donor) and pendant acceptor. The further increase in the length of the alkyl linkers in PBI-based double-cable polymers was found to show an unusual non-linear behavior, in which the donor/acceptor distance was observed to decrease with increasing length of the alkyl spacer before increasing again [39]. Similar behavior was also observed in naphthalene diimide (NDI)-based double-cable polymers [40]. The ability to tune the spacer length and hence the distance between donor and acceptor units in double-cable polymers also provides a convenient route to study the photoelectric conversion process [26]. Near-infrared electron acceptors usually use the strong electron-withdrawing 2-(3-oxo-2,3-dihydroinden-1-ylidene)malononitrile (IC) unit as the end group, which have been successfully applied into BHJOSCs. As different from PBI and NDI acceptors with face-to-face stacking structures, IC-based electron acceptors show three-dimensional networks [41–43]. Therefore, their introduction into double-cable polymers is expected to show different behavior in morphology, hence motivating this study into the linker effect on the morphology of IC-based double-cable polymers.

With this background, we systematically investigate the influence of alkyl linker length on the photovoltaic performance of near-infrared double-cable polymers in this work. A series of IC-based double-cable polymers, denoted as **Px** (x = 8, 10, 12, 14, 16), with varying lengths of the alkyl linker ranging from C_8H_{16} to $C_{16}H_{32}$, are synthesized for SCOSCs. Among these, the linker length x = 12 (**P12**) is found to optimize the power conversion efficiencies (PCEs) in SCOSCs. Specifically, PCEs increase from **P8** (7.83%) to **P10** (8.86%), reaching a peak at **P12** (10.09%), and then decrease from **P14** (8.05%) to **P16** (7.53%). Comprehensive investigations involving optical absorption, charge transport, and morphology analysis provide valuable insights into the underlying factors driving the observed variations in PCEs. Notably, the double-cable conjugated polymer **P12** exhibits a delicate balance between enhanced charge separation facilitated by the increased spacer length and reduced crystallinity resulting from longer spacers, higher charge mobilities, and well-balanced hole/electron transport characteristics, which account for the exceptional photovoltaic performance observed in SCOSCs based on **P12**.

The chemical structures of the double-cable conjugated polymers **Px** are shown in Fig. 1a, with the detailed synthetic routes provided in Supporting information. Polymer **P12** has been reported in our previous work [29], and similar procedures were used to synthesize the remaining double-cable polymers. In general, the key monomer of **M11x** is synthesized by a two-step bromination of the hydrogen-lithium exchange reaction/the bromination of CBr_4 at the α-position of the benzodithiophene unit and the bromination of hydrobromic acid on the methoxy group at the end of the alkyl chain. **M12x** monomer was obtained by Knoevenagel condensation of TPD dialdehyde with alkyl bromide. Finally, under the same reaction conditions, these double-cable conjugated polymers **Px**s were obtained by Stille polymerization based on **M12x** and **M13**. All polymers can be well dissolved in common organic solvents such as chlorobenzene (CB), *o*-dichlorobenzene (*o*-DCB) and trichlorobenzene (TCB). The molecular weights of the polymers were determined by gel permeation chromatography (GPC) with TCB as the eluent at 140 °C. The number average molecular weights (M_ns) of these polymers are in the range of 72.3-138.3 kDa (Fig. S1 and Table S1 in Supporting information), and the molar mass distributions ($Đ_M$) are 1.38-2.56.

Table 1
Photophysical properties of the double-cable polymer **Px**s.

Samples	λ_{onset}^{sol} (nm) [a]	λ_{onset}^{film} (nm) [b]	E_g^{film} (eV) [c]
P8	777	817	1.52
P10	779	819	1.51
P12	779	831	1.49
P14	774	828	1.50
P16	771	824	1.51

[a] Absorption maximum in thin films.
[b] Absorption maximum in thin films.
[c] Optical bandgap calculated from the onset absorption edge of thin films.

Table 2
Photovoltaic parameters of the optimized SCOSC devices based on different double-cable polymer **Px**s.

Polymer	V_{OC} (V)	J_{SC} (mA/cm^2)	J_{EQE} (mA/cm^2) [a]	FF (%)	PCE (%) [b]
P8	0.794	18.2	17.3	54.3	7.83 (7.68±0.08)
P10	0.772	19.3	18.6	59.3	8.86 (8.82±0.02)
P12	0.767	21.2	20.5	62.3	10.09 (10.00±0.06)
P14	0.762	18.2	18.4	57.9	8.05 (8.00±0.04)
P16	0.759	18.1	18.1	54.8	7.53 (7.39±0.10)

[a] J_{EQE} was calculated from the EQE integration.
[b] The values outside and inside the parentheses represent the optimal PCEs and the average PCEs with their corresponding standard deviations, respectively, which were calculated based on six individual devices.

The absorption spectra of the double-cable polymers, donor polymer PBDB-T, and acceptor molecule TPDIC are depicted in Fig. 1b (in chloroform solution) and Fig. 1c (in thin films), while the associated data are summarized in Table 1. In solution, all polymers exhibit similar absorption spectra, displaying significant absorption within the 500-800 nm range, attributable to the presence of donor backbones and acceptor side units. Notably, a distinct red shift in wavelength is observed when transitioning from solution to thin film. For instance, **P12** experiences a redshift of approximately 52 nm. Plotting the onset wavelength against different polymers in Fig. 1c reveals a red shift from **P8** to **P12**, followed by a blue shift from **P12** to **P16**, indicating variations in polymer aggregations and optical bandgaps (E_gs).

SCOSCs were fabricated with an inverted device structure of ITO/ZnO/**Px**s/MoO_3/Ag to examine the influence of alkyl linker length on photovoltaic properties. To ensure polymer solubility, *o*-DCB was chosen as the main solvent due to its high solubility with all **Px**s. An additive of 4% 1,8-diiodooctane (DIO) was incorporated into polymer films based on previous research [29]. During the spin coating process, the active layer thickness was carefully controlled between 65 nm and 75 nm to optimize device performance. A detailed description of the fabrication process can be found in Supporting information. Fig. 2a illustrates the optimized current density versus bias voltage (*J*-*V*) curves for SCOSCs based on various double-cable polymers **P8-P16** under simulated AM1.5G illumination. Photovoltaic parameters are summarized in Table 2 and Tables S2–S6 (Supporting information). An interesting parabolic-type trend of PCE as a function of alkyl spacer length was observed, which is similar to the trend in previous PBI-based

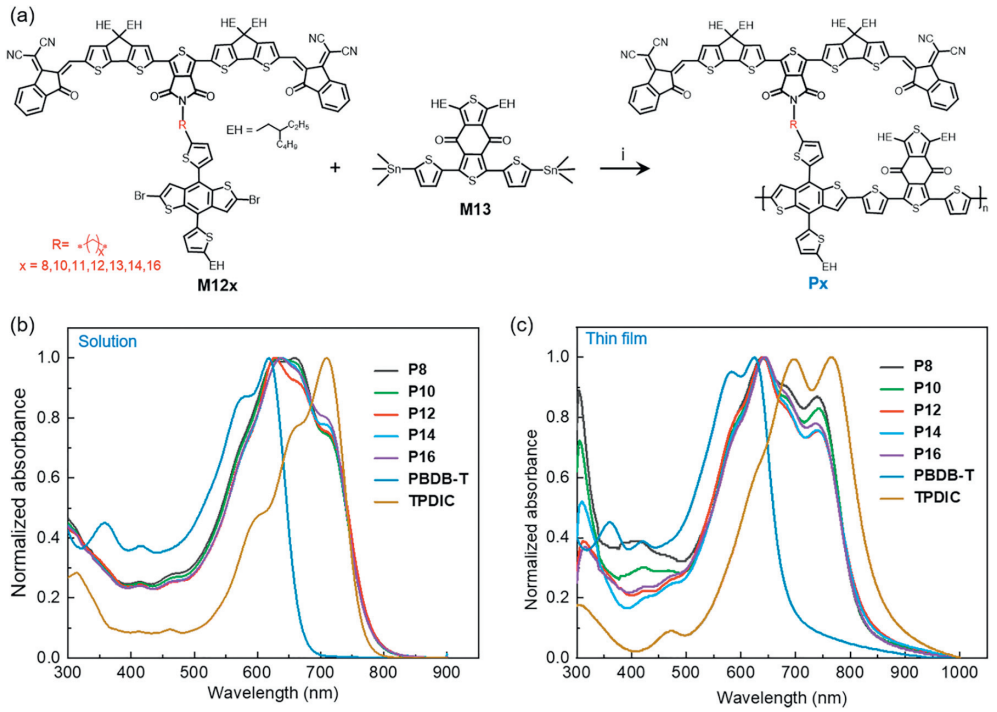

Fig. 1. (a) The chemical structures of the double-cable conjugated polymer **Px**s and their synthetic routes. (i) Stille polymerization, $Pd_2(dba)_3$/P(*o*-tolyl)$_3$, toluene, 115 °C, 12 h. Normalized absorption spectra of the double-cable polymers in (b) chloroform solution and (c) thin films.

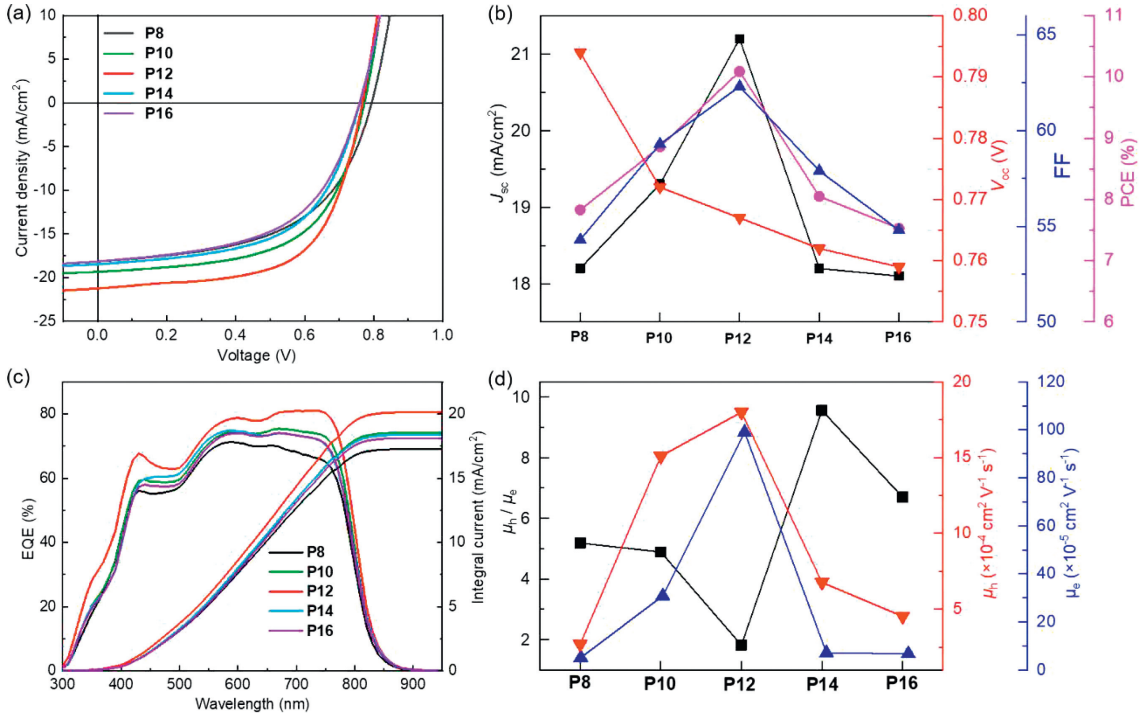

Fig. 2. (a) Optimized *J-V* characteristic curves for SCOSCs based on the double-cable polymers **P8**-**P16** under simulated AM1.5G illumination. J_{SC}, V_{OC}, and FF values (b) and EQE spectra (c) of the optimized SCOSC devices based on different polymers. The integrated current densities are also included. (d) Hole and electron mobilities of these polymers.

and NDI-based double-cable polymer systems [39,40]. Specifically, the champion PCE of the Px-based SCOSCs is observed to increase from 7.83% for **P8** to 8.86% for **P10**, reaching a peak of 10.09% for **P12** and then decreasing to 8.05% for **P14**, and further decreasing to 7.53% for **P16**. Notably, SCOSCs based on **P12** display the highest PCE of 10.09%, accompanied by an open-circuit voltage (V_{OC}) of 0.767 V, a short-circuit current density (J_{SC}) of 21.2 mA/cm^2, and a fill factor (FF) of 62.3%.

Further analysis was focused on the photovoltaic parameters, including V_{OC}s, J_{SC}s, and FF values as a function of linker lengths (Fig. 2b). Remarkably, it was observed that the V_{OC}s exhibited a decreasing trend from **P8** (0.794 V) to **P16** (0.759 V) with an in-

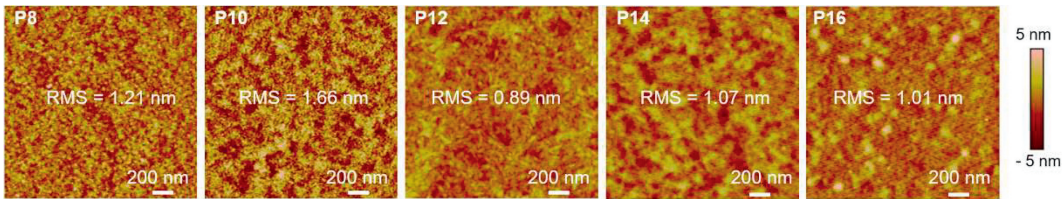

Fig. 3. AFM height images for all **Px** thin films.

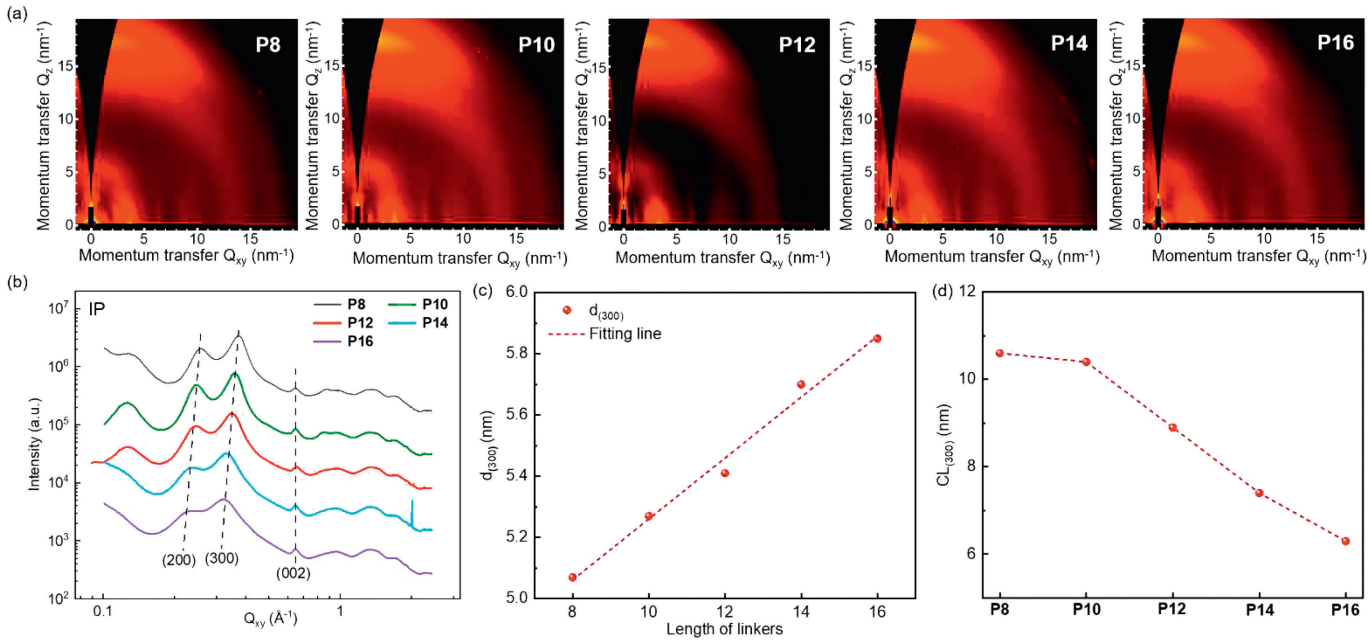

Fig. 4. 2D GIWAXS patterns (a) and the corresponding 1D IP plots (b) of the double-cable conjugated polymers. (c) *d*-spacings of the 300 peaks for different polymers. (d) Calculated CL values based on the (300) peaks versus different **Px** polymers.

crease in linker length, which is consistent with the trend reported in previous PBI-based polymer systems [35]. The J_{SC}s and FF values show similar variation trends with PCEs. Specifically, J_{SC}s increased from 18.2 mA/cm^2 for **P8**, to 19.3 mA/cm^2 for **P10**, peaking at 21.2 mA/cm^2 for **P12**, and then decreasing to 18.2 mA/cm^2 for **P14** and further to 18.1 mA/cm^2 for **P16**. The FF values exhibited a similar trend, rising from 54.3% for **P8** to 59.3% for **P10**, reaching a peak of 62.3% for **P12**, and subsequently decreasing to 57.9% for **P14** and further to 54.8% for **P16**. The discrepancies in J_{SC}s were also reflected in the external quantum efficiencies (EQEs) depicted in Fig. 2c.

To investigate the trends in J_{SC}s and FF values, we conducted space charge-limit current (SCLC) measurements to examine the vertical charge transport characteristics of the **Px** films. The *J-V* curves for hole-only and electron-only devices are presented in Figs. S2 and S3 (Supporting information). The calculated hole mobilities (μ_hs) and electron mobilities (μ_es) for all films based on **P8-P16** are shown in Fig. 2d and Table S1. The μ_h values increase from 2.7×10^{-4} cm^2 V^{-1} s^{-1} for **P8**, to 1.5×10^{-3} cm^2 V^{-1} s^{-1} for **P10**, reaching a peak of 1.8×10^{-3} cm^2 V^{-1} s^{-1} for **P12**, and then decreasing to 6.8×10^{-4} cm^2 V^{-1} s^{-1} for **P14**, and further still to to 4.5×10^{-4} cm^2 V^{-1} s^{-1} for **P16**. Similar trends are observed for μ_e values which can be attributed to differences in charge mobilities and light absorption characteristics of the photoactive layers. Additionally, the μ_h/μ_e ratios were calculated (Fig. 2d and Table S1), exhibiting a similar trend with FF and reaching the lowest value at **P12** (1.82), thereby explaining the variations in FF values.

We then studied the morphology of the polymer thin films *via* atomic force microscopy (AFM) and grazing-incidence wide-angle X-ray scattering (GIWAXS) measurements. As depicted in Fig. 3, the height images of AFM for all the polymers show smooth surfaces with similar root-mean-square roughness (RMS) values in the range of 0.89-1.66 nm, revealing excellent film-forming ability. GIWAXS measurements were further performed to investigate the evolution in the molecular packing and crystallinity of these polymer films with the 2D GIWAXS patterns (Fig. 4a) and the corresponding 1D out-of-plane (OOP, Fig. S4 in Supporting information) and in-plane (IP, Fig. 4b) plots. The appearance of (*h*00) peaks in the IP direction and (010) peaks in the OOP direction indicates that these polymers exhibit a preferentially face-on orientation, in which the polymer backbones are parallelly aligned to the substrates. As shown in Fig. S4 and Table S7 (Supporting information), all **Px** polymers possess a close π-π distance of 3.6 Å and similar intensity of (010) peaks, indicating that all **Px**s possess a similar degree of π-π stacking mode [29]. Another interesting observation is that the d-spacing values of the side-chain stacking periodicity (based on the (300) peaks which are the strongest and most reliable to fit) of the polymers have a significant linear increase from P8 to P16 (Fig. 4c), which is consistent with previous NDI-based double-cable polymers but different with previous PBI-based double-cable polymers [39,40]. To examine differences in the degree of crystallinity in these polymers, we calculated the coherence length (CL) values corresponding along the side-chain stacking direction based on the (300) peaks of these **Px** polymers, which are shown in Fig. 4d and summarized in Table S7. The CL values in general show a downward trend with increasing alkyl linker length, suggesting that polymers with increasing length of alkyl linkers have lower crystallinity (*i.e.*, smaller crystallite size or in-

creased crystalline disorder). **P12** may then represent a balance between improved charge separation facilitated by increased spacer length and increased crystalline disorder due to longer spacers.

In summary, we systematically investigated the influence of alkyl linker lengths on the photovoltaic performance of near-infrared double-cable polymers in SCOSCs. Five near-infrared double-cable polymers with varying alkyl linker lengths from C_8H_{16} to $C_{16}H_{32}$ were synthesized. The investigation revealed a parabolic-type distribution in PCEs, where the **P12**-based SCOSC shows the optimal PCE of 10.09%, and PCEs increase from **P8** to **P12** and then decline from **P12** to **P16**. Comprehensive analyses including optical absorption, charge transfer, and morphology provided valuable insights into the underlying factors driving these variations. It was found that the double-cable conjugated polymer **P12** exhibited a delicate balance between enhanced charge separation facilitated by the increased spacer length and increased crystalline disorder resulting from longer spacers, higher charge mobilities, and well-balanced hole/electron transport characteristics, accounting for the exceptional photovoltaic performance observed in **P12**-based SCOSC devices. This work highlights the significant impact of alkyl linker length on the photovoltaic performance of double-cable conjugated polymer-based SCOSCs. It also provides valuable insights and guidance for the design of new double-cable conjugated polymers.

Declaration of competing interest

The authors declare that they have no known competing financial interests or personal relationships that could have appeared to influence the work reported in this paper.

Acknowledgments

This study is jointly supported by the Beijing Natural Science Foundation (Nos. 2212045 and JQ21006) and the National Natural Science Foundation of China (Nos. 21905158, 52073016 and 92163128). This work was further supported by the Fundamental Research Funds for the Central Universities (Nos. buctrc202111, buctrc201828, and XK1802-2), the Opening Foundation of State Key Laboratory of Organic-Inorganic Composites of Beijing University of Chemical Technology (No. oic-202201006) and Jiangxi Provincial Department of Science and Technology (Nos. 20202ACBL213004, 20212BCJ23035, jxsq2019102004). This work was performed in part on the SAXS/WAXS beamline at the Australian Synchrotron, part of ANSTO.

Supplementary materials

Supplementary material associated with this article can be found, in the online version, at doi:10.1016/j.cclet.2023.109164.

References

[1] W. Lai, C. Li, J. Zhang, et al., Chem. Mater. 29 (2017) 7073–7077.
[2] Y. He, T. Heumuller, W. Lai, et al., Adv. Energy Mater. 9 (2019) 1900409.
[3] J. Roncali, I. Grosu, Adv. Sci. 6 (2019) 1801026.
[4] S. Liang, X. Jiang, C. Xiao, et al., Acc. Chem. Res. 54 (2021) 2227–2237.
[5] S. Liang, W. Li, L. Ding, J. Semicond. 44 (2023) 030201.
[6] G. Chamberlain, Sol. Cells 8 (1983) 47–83.
[7] D. Zhou, X. Cheng, H. Xu, et al., J. Mater. Chem. A 4 (2016) 18478–18489.
[8] D. Xia, S. Zhou, W.L. Tan, et al., Aggregate 4 (2022) e279.
[9] G. Zhang, Q. Chen, Z. Zhang, et al., Angew. Chem. Int. Ed. 62 (2023) 202216304.
[10] C. Zhao, Z. Zhang, F. Han, et al., Angew. Chem. Int. Ed. 60 (2021) 8526–8531.
[11] W. Gao, F. Qi, Z. Peng, et al., Adv. Mater. 34 (2022) e2202089.
[12] Y. Wei, Z. Chen, G. Lu, et al., Adv. Mater. 34 (2022) e2204718.
[13] G.Y. Ding, T.Y. Chen, M.T. Wang, et al., Nano-Micro Lett. 15 (2023) 14.
[14] G. Ding, T. Chen, M. Wang, et al., Nano-Micro Lett. 15 (2023) 92.
[15] J. Fu, P.W.K. Fong, H. Liu, et al., Nat. Commun. 14 (2023) 1760.
[16] C. Han, J. Wang, S. Zhang, et al., Adv. Mater. 35 (2023) e2208986.
[17] J. Wang, Y. Wang, P. Bi, et al., Adv. Mater. 35 (2023) e2301583.
[18] L. Zhu, M. Zhang, J. Xu, et al., Nat. Mater. 21 (2022) 656–663.
[19] A. Kiriy, V. Senkovskyy, M. Sommer, Macromol. Rapid Commun. 32 (2011) 1503–1517.
[20] D. Wang, Z.F. Yang, F. Liu, et al., Chin. Chem. Lett. 33 (2022) 466–469.
[21] C.S. Yu, Y.H. Xu, C. Li, et al., Chin. J. Chem. 36 (2018) 515–518.
[22] C.W. Zhao, Y.T. Guo, Y.F. Zhang, et al., J. Mater. Chem. A 7 (2019) 10174–10199.
[23] C. Li, C. Wang, Y.T. Guo, et al., J. Mater. Chem. C 7 (2019) 3802–3810.
[24] B.Q. Liu, Y.H. Xu, F. Liu, et al., Chin. J. Polym. Sci. 40 (2022) 898–904.
[25] H.S. Fang, D.D. Xia, C.W. Zhao, et al., Dyes Pigments 203 (2022) 110355.
[26] S. Liang, J. Wang, Y. Ouyang, et al., Macromolecules 55 (2022) 2517–2523.
[27] W. Lai, S. Karuthedath, C. Xiao, et al., Chin. Chem. Lett. 35 (2024) 108287.
[28] C. Wang, D. Xia, F. Yang, et al., ACS Appl. Polym. Mater. 3 (2021) 4645–4650.
[29] S. Liang, B. Liu, S. Karuthedath, et al., Angew. Chem. Int. Ed. 61 (2022) 202209316.
[30] B. Liu, S. Liang, S. Karuthedath, et al., Macromolecules 56 (2023) 1154–1164.
[31] B.Q. Liu, S.J. Liang, S. Karuthedath, et al., J. Mater. Chem. A 11 (2023) 12236–12244.
[32] X.Y. Xu, H.B. Wu, S.J. Liang, et al., Acta Phys. Chim. Sin. 38 (2022) 2201039.
[33] Z. Zhang, J. Wang, Z. Hu, et al., Chin. Chem. Lett. 34 (2023) 108527.
[34] S. Pang, X. Zhou, S. Zhang, et al., ACS Appl. Mater. Interfaces 12 (2020) 16531–16540.
[35] B.Q. Wu, Y. Zhang, S.Z. Tian, et al., Sol. RRL 6 (2022) 2101034.
[36] C.N. Gannett, L. Melecio-Zambrano, M.J. Theibault, et al., Mater. Rep. Energy 1 (2021) 100008.
[37] S. Li, C.Z. Li, M. Shi, H. Chen, ACS Energy Lett. 5 (2020) 1554–1567.
[38] S. Liang, C. Xiao, C. Xie, et al., Adv. Mater. 35 (2023) e2300629.
[39] G. Feng, W. Tan, S. Karuthedath, et al., Angew. Chem. Int. Ed. 60 (2021) 25499–25507.
[40] Z. Hu, C. Xiao, W. Tan, et al., Macromolecules 55 (2022) 5188–5196.
[41] L. Yuan, S. Liang, C. Xiao, et al., Chem. Asian J. 16 (2021) 4171–4178.
[42] C. Xiao, C. Li, F. Liu, et al., J. Mater. Chem. C 8 (2020) 5370–5374.
[43] D. Meng, J.L. Yang, C. Xiao, et al., Proc. Natl. Acad. Sci. U. S. A. 117 (2020) 20397–20403.